Supplementary Materials for "All-electrical Coherent Control of a Single Rare-earth Spin Qubit"

Yaowu Liu,[1,2,*†] Dasom Choi,[1,3,*] Stefano Reale,[1,2,*] Jeongmin Oh,[1,3]
Seorhin Choi,[1,3] Lei Fang,[1,2] We-hyo Soe,[1,2] Arzhang Ardavan,[4]
Andreas J. Heinrich,[1,3] Soo-hyon Phark,[1,2,‡] and Fabio Donati[1,3,§]

[1]*Center for Quantum Nanoscience (QNS),*
Institute for Basic Science (IBS), Seoul 03760, Republic of Korea
[2]*Ewha Womans University, Seoul 03760, Republic of Korea*
[3]*Department of Physics, Ewha Womans University, Seoul 03760, Republic of Korea*
[4]*Department of Physics, University of Oxford,*
The Clarendon Laboratory, Oxford OX1 3PU, U.K

Contents

I. Basic characterization of Er(B) S3

A. Topography and differential conductance S3

B. ESR on Er(B) S3

II. Transition energies of f_5 S5

III. Fitting ESR spectrum S6

IV. Decomposition of $|+\rangle$ state S8

V. Influence of tip-induced field S10

VI. Dependence of Rabi frequencies of f_1 and f_3 on tip-atom distance S11

VII. Spin dynamics of Er $4f$ spin S13

VIII. Multiplet calculations S14

IX. Coherent control mechanism S18

A. Modulation of diagonal components in $\mathcal{J}$ S19

B. Modulating the off-diagonal term through rotational modulation S21

C. Contribution of dipolar interaction S27

D. Special cases of coherent control mechanism: $\theta = 90°$, $\phi = 0°$ or $\phi = 90°$ S28

E. Special cases of coherent control mechanism: $\theta = 90°$, $0° < \phi < 90°$ S28

X. Readout process in Er-Ti pair S30

XI. Simulation of Er(O)-Ti pair S32

References S34

I. Basic characterization of Er(B)

A. Topography and differential conductance

Er(B) appears higher than both Er(O) and Ti(B) in STM topographic images acquired at $V_{\mathrm{DC}} = 100$ mV and $I_{\mathrm{DC}} = 20$ pA, with an apparent height of 265 pm, as highlighted by the blue circle in Fig. S1**a**. The differential conductance ($\mathrm{d}I/\mathrm{d}V$) spectra measured on Ti(B) and Er(B) with a spin-polarized tip are shown in Fig. S1**b**. Ti(B) exhibits a clear spin-polarized signature, manifested as a step-like feature around zero bias. By contrast, the $\mathrm{d}I/\mathrm{d}V$ spectra measured on Er(B) show no observable spin excitation or spin-polarized contrast[1], consistent with the closed-shell character of its outer electronic states.

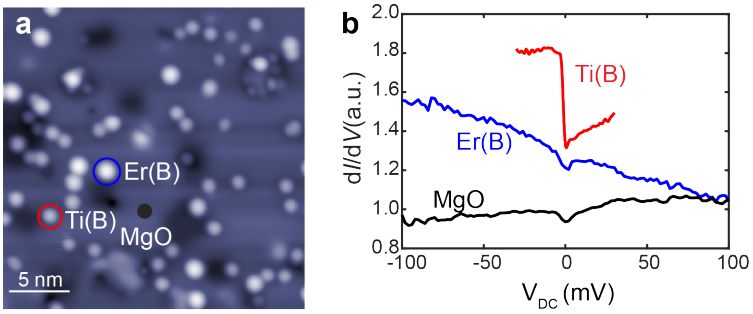

FIG. S1. **Topography and differential conductance of Er(B) and Ti(B). a,** STM topographic image of a MgO patch with Er, Ti and Fe atoms ($V_{\mathrm{DC}} = 100$ mV, $I_{\mathrm{DC}} = 20$ pA, 20 nm $\times$ 20 nm). An Er(B) and a Ti(B) atoms are marked by the blue and red circles, respectively. **b,** Differential conductance spectra using a spin-polarized tip on Er(B), Ti(B) and MgO in (**a**) ($V_{\mathrm{DC}} = 100$ mV (blue and black curves) and 30 mV (red curve), $I_{\mathrm{DC}} = 200$ pA, $V_{\mathrm{osc}} = 1$ mV, $\boldsymbol{B}_{\mathrm{ext}} = 0.25$ T, $\theta = 90°$ and $\phi = 52°$).

B. ESR on Er(B)

Here we provide ESR spectra on both atoms in an Er-Ti pair. Figure S2 shows a featureless spectrum when we place the tip on Er(B), which is due to the closed outer electron shell of an Er atom on an ultrathin MgO surface.

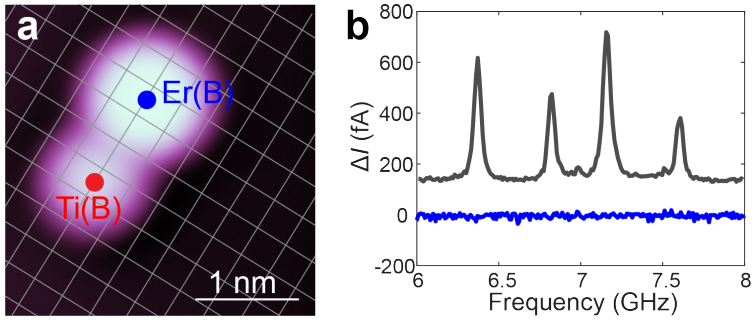

FIG. S2. **ESR spectra on Er(B) and Ti(B). a,** STM topography of an Er-Ti pair (V_{DC} = 100 mV, I_{DC} = 20 pA, 3 nm× 3 nm). The gray grid represents the MgO lattice with the crossing points representing oxygen atomic sites on the surface layer. **b,** ESR spectra at the two spots in (**a**) (V_{DC} = 100 mV, I_{DC} = 20 pA, V_{RF} = 20 mV, $\boldsymbol{B}_{\mathrm{ext}}$ = 0.25 T, $\theta = 90°$ and $\phi = 52°$).

II. Transition energies of f_5

As shown in Fig. S3, the transition energy of f_5 remains locked to the two-transition sum, $f_1 + f_4$ or equivalently $f_2 + f_3$, over the entire polar-angle θ sweep.

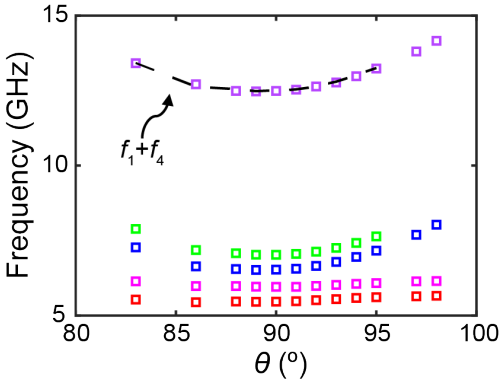

FIG. S3. **Double-quantum transition f_5.** ESR peak position for each transition shown in Fig. 1**c** in the manuscript.

III. Fitting ESR spectrum

In this section, we describe the fitting procedure used to analyze the ESR spectra presented in Fig. 4 of the main text, from which we extract the effective exchange interaction and the anisotropic $\mathfrak{g}$-tensor. To determine the effective g factors of Er on the two-monolayer MgO surface, we map the ground-state doublet of Er to an effective spin-1/2 degree of freedom, denoted by $\boldsymbol{S}_{\mathrm{Er}}$. Within this effective-spin description, the Er-Ti pair is described by a spin Hamiltonian consisting of the Zeeman term $\mathcal{H}_{\mathrm{Z}}$ and the spin-spin interaction term $\mathcal{H}_{\mathrm{int}}$:

$$\mathcal{H} = \mathcal{H}_{\mathrm{Z}} + \mathcal{H}_{\mathrm{int}} = -\mu_{\mathrm{B}} \boldsymbol{S}_{\mathrm{Ti}} \cdot \mathfrak{g}^{\mathrm{Ti}} \cdot (\boldsymbol{B}_{\mathrm{ext}} + \boldsymbol{B}_{\mathrm{tip}}) - \mu_{\mathrm{B}} \boldsymbol{S}_{\mathrm{Er}} \cdot \mathfrak{g}^{\mathrm{Er}} \cdot \boldsymbol{B}_{\mathrm{ext}} + \boldsymbol{S}_{\mathrm{Ti}} \cdot \mathcal{J} \cdot \boldsymbol{S}_{\mathrm{Er}}, \quad (1)$$

with μ_{B} the Bohr magneton, $\boldsymbol{B}_{\mathrm{ext}}$ the external magnetic field, $\boldsymbol{B}_{\mathrm{tip}}$ the magnetic field from the tip, $\mathfrak{g}^{\mathrm{Ti(Er)}}$ the $\mathfrak{g}$-tensor for Ti (Er) spin and $\mathcal{J}$ the spin interaction tensor. As in previous works, the effective tip field $\boldsymbol{B}_{\mathrm{tip}}$ only applies to the spin under the tip, in this case Ti[2]. The $\mathcal{H}_{\mathrm{int}}$ term can be decomposed into exchange and dipole-dipole contributions:

$$\mathcal{H}_{\mathrm{exc}} = \boldsymbol{S}_{\mathrm{Ti}} \cdot \mathcal{J}^{\mathrm{exc}} \cdot \boldsymbol{S}_{\mathrm{Er}}, \quad (2)$$

$$\mathcal{H}_{\mathrm{dip}} = \frac{\mu_0 \mu_B^2}{4\pi r^3} [(\mathfrak{g}^{\mathrm{Ti}} \cdot \boldsymbol{S}_{\mathrm{Ti}}) \cdot (\mathfrak{g}^{\mathrm{Er}} \cdot \boldsymbol{S}_{\mathrm{Er}}) - 3(\hat{r} \cdot \mathfrak{g}^{\mathrm{Ti}} \cdot \boldsymbol{S}_{\mathrm{Ti}})(\hat{r} \cdot \mathfrak{g}^{\mathrm{Er}} \cdot \boldsymbol{S}_{\mathrm{Er}})]. \quad (3)$$

Here $\hat{r}$ is the unit vector connecting the two spins and $\mathcal{J}^{\mathrm{exc}}$ is the exchange tensor. In this model, we assume that the tip-induced magnetic field, $\boldsymbol{B}_{\mathrm{tip}}$, follows the direction of the external magnetic field. The experimental data are fitted using this Hamiltonian, with both the transition energies and the normalized Rabi frequencies included in the fitting procedure. Here, the Rabi frequencies are normalized by the Rabi frequency of the f_3 transition at $\theta = 90°$ and $\phi = 52°$, as shown in Fig. S13**c**. Including the Rabi frequencies provides direct constraints on the driving matrix elements, thereby enabling a more stringent and physically faithful characterization of the microscopic driving mechanism.

Using this spin Hamiltonian, we fit the angular dependence of ESR transitions for the (3, 0) pair presented in Fig. 4 of the main text, and we obtain the Er $\mathfrak{g}$-tensor:

$$\mathfrak{g}^{\mathrm{Er}} = \begin{pmatrix} \mathfrak{g}_{xx}^{\mathrm{Er}} & 0 & 0 \\ 0 & \mathfrak{g}_{yy}^{\mathrm{Er}} & 0 \\ 0 & 0 & \mathfrak{g}_{zz}^{\mathrm{Er}} \end{pmatrix} \quad (4)$$

with $\mathfrak{g}_{xx}^{\mathrm{Er}} = 1.05 \pm 0.02$, $\mathfrak{g}_{yy}^{\mathrm{Er}} = 2.22 \pm 0.02$, and $\mathfrak{g}_{zz}^{\mathrm{Er}} = 9.59 \pm 0.04$. The fitted $\mathcal{J}^{\mathrm{exc}}$ from the fitting in MHz is:

$$\mathcal{J}^{\mathrm{exc}} = \begin{pmatrix} \mathcal{J}_{xx}^{\mathrm{exc}} & 0 & 0 \\ 0 & \mathcal{J}_{yy}^{\mathrm{exc}} & 0 \\ 0 & 0 & \mathcal{J}_{zz}^{\mathrm{exc}} \end{pmatrix} \tag{5}$$

with $\mathcal{J}_{xx}^{\mathrm{exc}} = 79.6 \pm 5.5$ MHz, $\mathcal{J}_{yy}^{\mathrm{exc}} = 543.7 \pm 6.3$ MHz, and $\mathcal{J}_{zz}^{\mathrm{exc}} = 1272.5 \pm 7.8$ MHz.

IV. Decomposition of $|+\rangle$ state

In this section, we examine how the spin character of the f_3 transition evolves with the polar angle θ, while keeping the azimuthal angle fixed at $\phi = 52°$. We first calculate the eigenstates of the effective spin-1/2 Hamiltonian in Eq. (1), including the full spin-spin interaction with fitted $\mathcal{J}$ and $\mathfrak{g}^{\mathrm{Er}}$ tensors, and label the four resulting energy eigenstates as $|00\rangle$, $|-\rangle$, $|+\rangle$, and $|11\rangle$, following the notation used in the main text. We then calculate the eigenstates of the corresponding non-interacting Hamiltonian, for which the eigenstates are pure Zeeman product states denoted by $|00\rangle$, $|10\rangle$, $|01\rangle$, and $|11\rangle$.

To quantify the Er contribution to the f_3 transition, we evaluate the overlap

$$P = |\langle +|01\rangle|^2, \tag{6}$$

as shown in Fig. S4. At $\theta = 83°$ and $\phi = 52°$, which is the field condition for the Rabi data presented in Fig. 2 of the main text, we find that the $|+\rangle$ state has predominantly Er character, containing 96% Er-like character and only 4% Ti-like character.

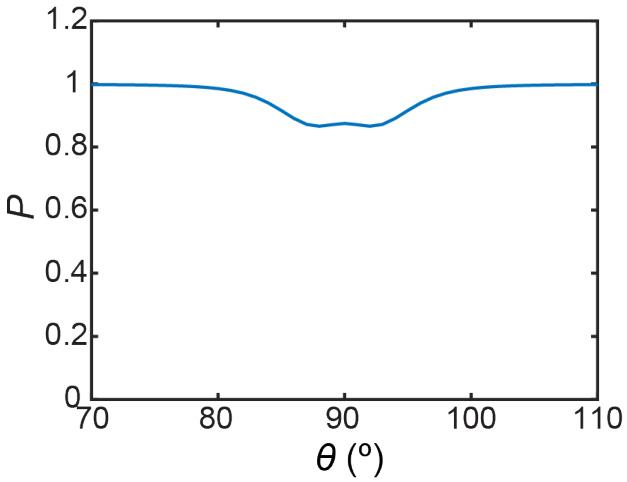

FIG. S4. **Decomposition of $|+\rangle$ state.** $P = |\langle +|01\rangle|^2$ as a function of polar angle θ with azimuthal angle fixed at 52°, $\boldsymbol{B}_{\mathrm{ext}} = 0.25$ T.

Note that the Rabi rate map for SQT Er in Fig. 5 of the main text is obtained at each field direction by:

$$\Omega = \langle 00|\, \mathcal{H}_{\mathrm{drive}}\, |01\rangle \tag{7}$$

where $|01\rangle$ is the pure Zeeman energy state described above and $\mathcal{H}_{\text{drive}}$ is the driving Hamiltonian, which will be discussed in the following sections.

V. Influence of tip-induced field

In Fig. S5, we show that the tip-induced magnetic field has a pronounced influence on the transition energies of f_1 and f_2, while its effect on f_3 and f_4 is negligible under the field condition used in Figs. 1 and 2 of the main text ($\boldsymbol{B}_{\mathrm{ext}} = 0.25$ T, $\theta = 83°$, and $\phi = 52°$). This suggests that f_1 and f_2 are predominantly Ti transitions while f_3 and f_4 are predominantly Er transitions.

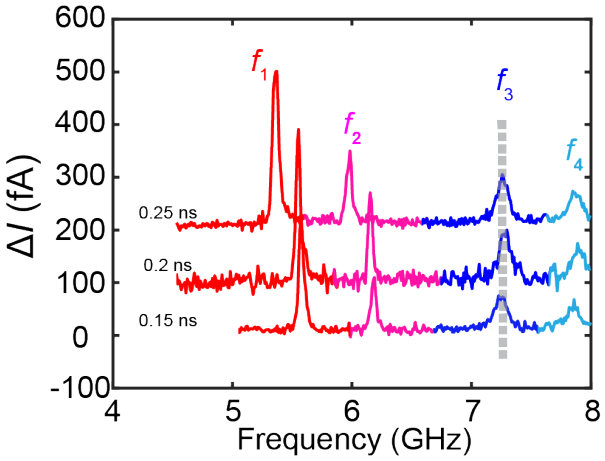

FIG. S5. **Influence of tip-induced field.** ESR spectra taken under the field condition of $\boldsymbol{B}_{\mathrm{ext}} = 0.25$ T, $\theta = 83°$ and $\phi = 52°$ as a function of tip-atom distance parameterized by the conductance. All data were taken using an RF voltage of $V_{\mathrm{RF}} = 20$ mV.

VI. Dependence of Rabi frequencies of f_1 and f_3 on tip-atom distance

To investigate the influence of the tip on the Rabi frequency of the Ti-like transition f_1 and the Er-like transition f_3, we performed Rabi measurements on f_1 and f_3 with different tip-Ti distances ($V_{\mathrm{RF}} = 100$ mV, $\boldsymbol{B}_{\mathrm{ext}} = 0.25$ T, $\theta = 83°$, $\phi = 52°$). As shown in Fig. S6, when the tip approaches closer to the Ti atom, the Rabi frequency first increases and then decreases. In contrast, for the f_3 transition, the Rabi oscillation frequency does not exhibit a clear correlation with the tip-Ti atom distance, consistent with the discussion in the main text. The extracted Rabi frequency as a function of conductance is shown in Fig. 2(**e**) of the main text.

As the tip initially approaches the Ti atom, the enhanced exchange interaction between the spin-polarized tip and the Ti spin increases the effective driving field[3], leading to an enhancement of the Rabi frequency of the f_1 transition. In this regime, the dominant effect is the strengthening of the transverse driving component mediated by the tip polarization. However, when the tip is brought even closer, the tip-induced exchange field becomes sufficiently strong to modify the quantization axis of the Ti spin. This additional static polarization effect alters the spin eigenbasis and can consequently change the effective transverse driving amplitude. As a result, the Rabi frequency no longer follows a simple monotonic trend with conductance.

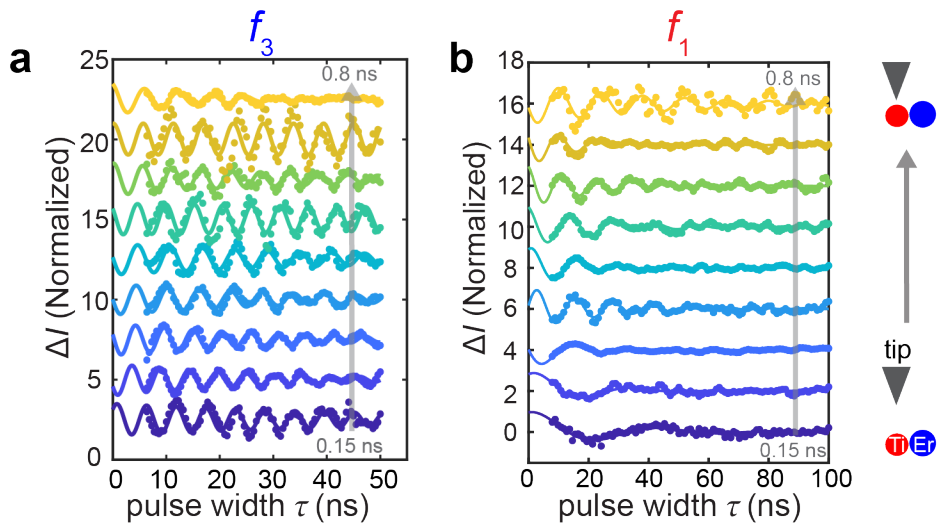

FIG. S6. **Rabi oscillations of f_1 and f_3 with different tip-Ti atom distances.** **a,** Rabi oscillations for f_3 with different conductances. **b,** Rabi oscillation for f_1 with different conductance. All data were taken with $V_{\mathrm{RF}} = 100$ mV, $\boldsymbol{B}_{\mathrm{ext}} = 0.25$ T, $\theta = 83°$, $\phi = 52°$.

VII. Spin dynamics of Er $4f$ spin

In this section, we present the spin dynamics of the Er $4f$ spin. We performed a standard spin-echo measurement on the f_3 transition under the magnetic-field condition ($\boldsymbol{B}_{\mathrm{ext}} = 0.25$ T, $\theta = 90°$, $\phi = 52°$). From this measurement, we extracted an echo coherence time of $T_2^{\mathrm{Echo}} = 112.9 \pm 13.4$ ns, as shown in Fig. S7**b**. Using a recovery pulse sequence, we further measured the spin lifetime of the f_3 transition, obtaining $T_1 = 57.2 \pm 9.8$ ns, as presented in Fig. S7**c**. We attribute the relatively short coherence time and lifetime primarily to the presence of Ti as the coupling partner of Er. Replacing Ti with a different neighboring atom, such as Ho or Sm, may mitigate these limitations. Moreover, implementing an Er-Ho or Er-Sm pair as a remote qubit, read out via a Ti sensor spin, could substantially enhance the coherence properties of the system.

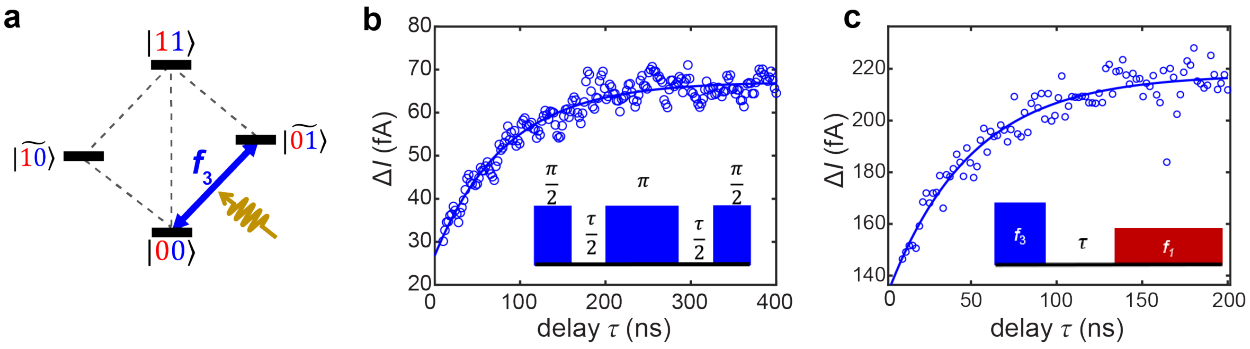

FIG. S7. **Er spin dynamics. a,** Energy diagram of Er-Ti. **b,** Spin-echo measurement performed on f_3 ($V_{\mathrm{DC}} = 100$ mV, $I_{\mathrm{DC}} = 20$ pA, $V_{\mathrm{RF}} = 30$ mV). **c,** Recovery-sequence measurement performed on f_3 ($V_{\mathrm{DC}} = 100$ mV, $I_{\mathrm{DC}} = 20$ pA, $V_{\mathrm{RF}} = 30$ mV for pumping f_3 and $V_{\mathrm{RF}} = 20$ mV for probing). All data were acquired under a magnetic-field condition of $\boldsymbol{B}_{\mathrm{ext}} = 0.25$ T, $\theta = 90°$, and $\phi = 52°$ ($f_{\mathrm{res}} = 6.51$ GHz).

VIII. Multiplet calculations

Quantum states of Er atoms were computed using the Quanty multielectron code[4]. Open-shell multiplet calculations were performed by modeling the intra- and inter-orbital electron-electron interactions using Slater integrals, whose values were obtained from the full-electron Cowan atomic structure code[5]. All Slater integrals were calculated assuming a $4f^{11}5d^2$ electronic configuration. The two electrons in the $5d$ shell were included to account for configuration interaction mediated by the ligand field, as discussed below. The Slater integrals were rescaled to account for screening effects arising from surface electrons. A reduction factor of 0.85 was adopted based on previous X-ray measurements[6]. In addition to electron-electron interactions, the Hamiltonian used for the multiplet calculations includes spin-orbit coupling, Zeeman energy due to the external magnetic field, crystal field effects acting on the different shells, and configuration-interaction ligand field terms acting on the outer $5d$ electrons. The spin-orbit coupling parameters were also computed using Cowan's atomic structure code[6]. The crystal field acting on the open valence shells of the lanthanide was modeled according to the symmetry and orbital character of the corresponding states.

For localized $4f$ electrons, we modeled the crystal field using a point-charge electrostatic model[7,8], including only the nearest neighbors of the adsorbed lanthanide atom. The positions of the neighboring ions surrounding the Er atom were obtained from DFT calculations[6], and the Born charges ($\pm 2e$ for Mg and O, respectively) were globally rescaled to account for mutual screening and the finite spatial extension of the ions. In addition, the radial extension of the $4f$ orbitals was renormalized by rescaling the radial operator as $\hat{r} \rightarrow \alpha\hat{r}$ to account for dielectric screening by surface electrons. The reduced charge (q_{red}) and the radial rescaling parameter (α) were treated as free parameters to fit the experimental $\mathfrak{g}$-tensor. To this end, the three principal values of the $\mathfrak{g}$-tensor were calculated from the Zeeman energy along the three principal axes by projecting onto a pseudo-spin 1/2 ground-state doublet. However, with only these two degrees of freedom, it was not possible to reproduce the experimentally measured $\mathfrak{g}$-tensor with satisfactory accuracy.

To address this limitation, we introduced a finite electron occupation of the $5d$ orbitals, which provides an additional anisotropic interaction acting on the $4f$ electrons. For the $5d$ shell, an artificially large crystal-field splitting (10 eV) was imposed to separate the $5d_{y^2}$ type

orbital from the remaining $5d$ orbitals. This choice isolates the orbital with maximal overlap toward the positively charged Mg atoms, which is expected to lie lowest in energy. Previous DFT studies of lanthanide atoms on MgO/Ag(100)[9,10] report a typical $5d$ occupation below one electron and no net polarization within this shell.

To reproduce this situation, we included a ligand-field term with configuration interaction between the $5d^0$ and $5d^2$ configurations. The exclusion of odd $5d$ configurations ensures negligible net polarization. The $5d$ occupation was tuned by fixing the hopping parameter to 0.5 eV and treating the on-site energy Δ as an additional free parameter in the fit. The fitting procedure was performed using Bayesian optimization as implemented in MATLAB. The error function was defined as the squared difference between calculated and experimental principal values of the Er $\mathfrak{g}$-tensor. The parameters reported in Fig. 4 of the main text correspond to the best-fit values $\alpha = 1.155$, $q_{\mathrm{red}} = 0.5932$, and $\Delta = 6.6467$ eV, yielding a $5d$ occupation of 0.5344 electrons.

The eigenstates of the lowest ${}^4I_{15/2}$ multiplet split due to the combination of crystal field from the point charge and electrostatic interaction with the $5d$ electron into a set of doublets, whose angular momentum distribution is best visualized by projecting along the oxygen direction (x). Along this axis (Fig. S8), the eigenstates form an upturned parabola representative of a hard axis. Similar to Er(O), the lowest two states are minimally projected along the quantization axis, although the two atoms have different hard axis directions, namely, out-of-plane for Er(O)[1,6] and in-plane along O-O direction for Er(B). The hard-axis anisotropy along the oxygen direction also appears in the $\mathfrak{g}$-tensor shown in Fig. 4**c** of the main text, where the x-component is the lowest among the three principal directions.

Minimally projected states in Kramers ions typically provide a natural two-level system to enable spin transitions through exchange of a single unit of angular momentum[1,6], which is the key to efficient quantum coherent control. To verify whether this holds for Er(B) multiplet states, we expand the eigenstates $|i\rangle$ from the full Hamiltonian over the free atom basis $|J = 15/2, m_J\rangle$ obtained by taking the quantization axis along the oxygen direction:

$$|i\rangle = \sum_j c_{ij} \, |J = 15/2, m_J\rangle \, . \tag{8}$$

The square moduli of the coefficients ($|c_{ij}|^2$) representing the relative weight of each $|J = 15/2, m_J\rangle$ in the Er(B) eigenstates are shown in Table I. In line with our expectation, the lowest doublet shows the largest weights on the $|J = 15/2, m_J = \pm 1/2\rangle$ states,

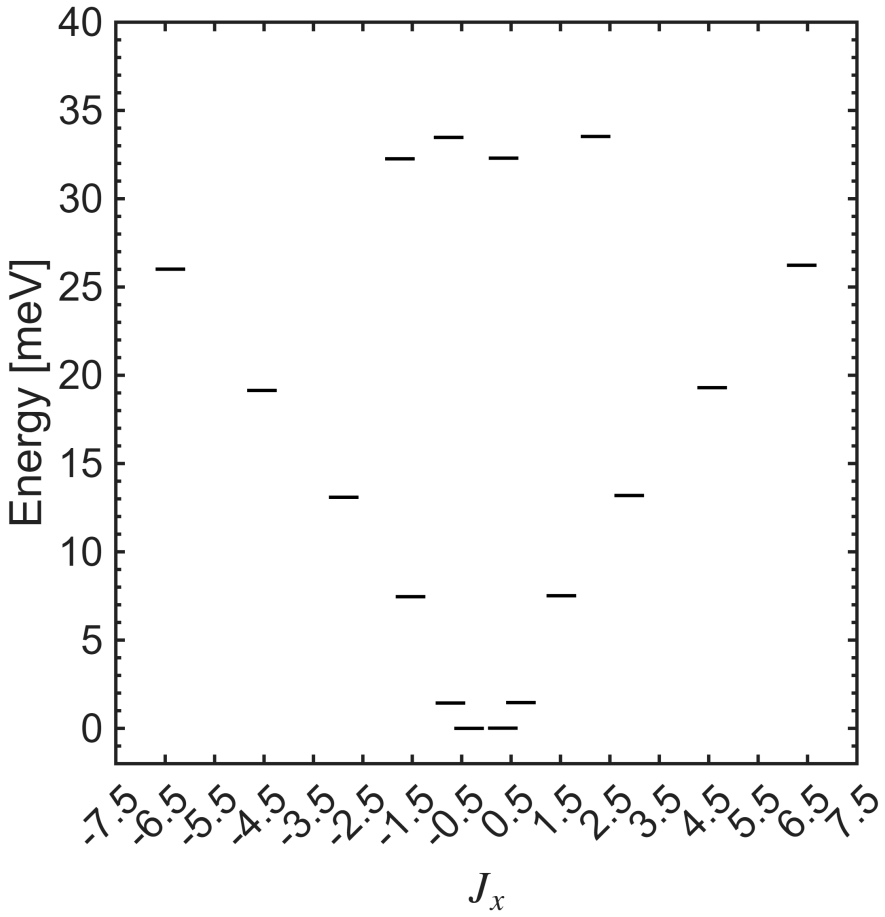

FIG. S8. **Quantum levels of Er(B)**. Eigenstates of the lowest $^4I_{15/2}$ multiplet of Er(B) versus their total angular moment projected along the oxygen x direction (J_x).

which enables efficient first-order ESR transitions. In addition, this decomposition further justifies modeling the ESR data with a spin Hamiltonian where the lowest two levels are mapped into an effective S = 1/2 system.

TABLE I. Eigenstates of Er(B) obtained using multiplet calculations. The left section shows the expectation values of the projected angular momentum along the oxygen direction J_x, the related magnetic moment μ_x, and the energy E in meV with respect to the ground state. The right section shows the relative weight $|c_{ij}|^2$ of the crystal-field eigenstates $|i\rangle$ expressed in the free atom $|J = 15/2, m_J\rangle$ basis, and calculated for a quantization axis along the oxygen direction with a magnetic field $\boldsymbol{B} = 0.25$ T along the x-axis ($\theta = 90°$ and $\phi = 0°$).

State	J_x	μ_x	E (meV)	m_J component weight ($\lvert c_{ij}\rvert^2$)															
				$-\frac{15}{2}$	$-\frac{13}{2}$	$-\frac{11}{2}$	$-\frac{9}{2}$	$-\frac{7}{2}$	$-\frac{5}{2}$	$-\frac{3}{2}$	$-\frac{1}{2}$	$\frac{1}{2}$	$\frac{3}{2}$	$\frac{5}{2}$	$\frac{7}{2}$	$\frac{9}{2}$	$\frac{11}{2}$	$\frac{13}{2}$	$\frac{15}{2}$
1	−0.350	0.419	0.000	0.0	0.0	0.0	0.0	0.0	10.1	0.0	79.8	0.0	2.6	0.0	7.0	0.0	0.4	0.0	0.0
2	0.333	−0.399	0.012	0.0	0.0	0.5	0.0	7.2	0.0	2.8	0.0	79.4	0.0	10.1	0.0	0.0	0.0	0.0	0.0
3	−0.728	0.872	1.435	0.0	0.0	0.0	0.0	5.1	0.0	68.8	0.0	11.6	0.0	11.4	0.0	3.0	0.0	0.0	0.0
4	0.699	−0.837	1.460	0.0	0.0	0.0	3.2	0.0	12.1	0.0	11.2	0.0	68.5	0.0	5.0	0.0	0.0	0.0	0.0
5	−1.535	1.840	7.459	0.0	1.8	0.0	22.6	0.0	48.0	0.0	0.3	0.0	9.9	0.0	14.8	0.0	2.5	0.0	0.0
6	1.518	−1.821	7.512	0.0	0.0	2.7	0.0	15.2	0.0	9.1	0.0	0.3	0.0	48.7	0.0	22.3	0.0	1.8	0.0
7	−2.887	3.461	13.090	1.1	0.0	35.6	0.0	36.0	0.0	11.9	0.0	3.4	0.0	0.8	0.0	8.6	0.0	2.7	0.0
8	2.891	−3.465	13.190	0.0	2.9	0.0	8.5	0.0	0.5	0.0	3.2	0.0	11.5	0.0	36.8	0.0	35.4	0.0	1.1
9	−4.542	5.441	19.140	0.0	53.3	0.0	19.1	0.0	18.4	0.0	3.0	0.0	2.0	0.0	0.1	0.0	3.6	0.0	0.5
10	4.570	−5.474	19.298	0.5	0.0	3.5	0.0	0.0	0.0	1.9	0.0	2.9	0.0	18.3	0.0	19.7	0.0	53.3	0.0
11	−6.396	7.654	26.011	71.7	0.0	10.5	0.0	13.7	0.0	2.2	0.0	0.5	0.0	0.2	0.0	0.1	0.0	1.1	0.0
12	6.382	−7.638	26.232	0.0	1.1	0.0	0.2	0.0	0.1	0.0	0.5	0.0	2.2	0.0	13.9	0.0	11.0	0.0	71.1
13	−1.750	2.094	32.262	0.0	30.2	0.0	32.3	0.0	6.2	0.0	0.3	0.0	0.1	0.0	5.1	0.0	14.6	0.0	11.2
14	0.348	−0.417	32.299	14.6	0.0	21.2	0.0	8.3	0.0	0.4	0.0	0.1	0.0	4.5	0.0	25.8	0.0	25.0	0.0
15	−0.764	0.914	33.474	12.1	0.0	26.0	0.0	14.5	0.0	3.0	0.0	1.8	0.0	6.1	0.0	20.5	0.0	16.0	0.0
16	2.211	−2.644	33.526	0.0	10.5	0.0	14.2	0.0	4.5	0.0	1.6	0.0	3.2	0.0	17.3	0.0	32.5	0.0	16.1

IX. Coherent control mechanism

As established in Figs. 2 and 3 in the main text, the effective field acting on the Er spin depends not only on the Er-Ti distance, but also on the direction of the Er-Ti bond. This indicates that the spin interaction should be described by an anisotropic exchange tensor whose value depends on both the relative position of the two atoms and their local orbital configurations. The static Hamiltonian for spin-spin interaction is:

$$\mathcal{H}_{\text{int}} = \boldsymbol{S}_{\text{Ti}} \mathcal{J} \boldsymbol{S}_{\text{Er}}, \tag{9}$$

where

$$\mathcal{J} = \mathcal{J}\left(\boldsymbol{r}, \boldsymbol{\eta}_{\text{Ti}}, \boldsymbol{\eta}_{\text{Er}}\right). \tag{10}$$

Here $\boldsymbol{r}$ is the vector connecting the Ti and Er atoms, while $\boldsymbol{\eta}_{\text{Ti}}$ and $\boldsymbol{\eta}_{\text{Er}}$ characterize the orientations of the Ti and Er ground-state orbitals with respect to the lattice.

Under RF excitation, the microscopic configuration of the Er-Ti pair is perturbed. We describe this perturbation as a time-dependent infinitesimal trajectory $X_{\text{RF}}(t)$ in the configuration space $\boldsymbol{q} = (\boldsymbol{r}, \boldsymbol{\eta}_{\text{Ti}}, \boldsymbol{\eta}_{\text{Er}})$. Because $\mathcal{J}$ is a rank-2 tensor acting in spin space, an RF-induced rotation of the local spin/orbital frames changes not only its components but also the spin basis in which those components are defined. Its modulation is therefore described by a covariant, or Lie-derivative, change rather than by an ordinary directional derivative alone. The complete first-order variation is given by the Lie derivative of $\mathcal{J}$ along the RF-induced trajectory,

$$\delta\mathcal{J}(t) = \mathcal{L}_{X_{\text{RF}}(t)} \mathcal{J}. \tag{11}$$

Consequently, the most general RF driving Hamiltonian to first order in the RF amplitude is

$$\mathcal{H}_{\text{d}}(t) = \boldsymbol{S}_{\text{Ti}} \left[\mathcal{L}_{X_{\text{RF}}(t)} \mathcal{J}\right] \boldsymbol{S}_{\text{Er}}. \tag{12}$$

The RF perturbation can change the exchange tensor in two physically distinct ways. First, it can modify the tensor components by changing the bond geometry or the local orbital configuration. Second, it can rotate the spin frames in which the tensor indices are defined, creating off-diagonal terms in $\mathcal{J}(\boldsymbol{q}(t))$. The Lie derivative provides a compact way to keep

track of both effects:

$$\mathcal{L}_{X_{\mathrm{RF}}(t)}\mathcal{J} = \underbrace{X_{\mathrm{RF}}(t)\cdot\nabla\mathcal{J}}_{\text{component change from geometry/orbital modulation}} + \underbrace{A_{\mathrm{Ti}}^{\mathsf{T}}(t)\mathcal{J}+\mathcal{J}A_{\mathrm{Er}}(t)}_{\text{rotation of the Ti and Er spin indices}} . \quad (13)$$

Here $A_{\mathrm{Ti}}(t)$ and $A_{\mathrm{Er}}(t)$ are the corresponding infinitesimal generators that rotate the Ti and Er spin frames. The first term is therefore the ordinary directional derivative of $\mathcal{J}$ along the RF trajectory, whereas the second term accounts for the fact that $\mathcal{J}$ is a rank-two tensor whose two spin indices transform with the local Ti and Er frames.

A. Modulation of diagonal components in $\mathcal{J}$

The first term in Eq. (13) can be written as

$$X_{\mathrm{RF}}(t)\cdot\nabla\mathcal{J} = \delta\boldsymbol{r}(t)\cdot\nabla_{\boldsymbol{r}}\mathcal{J} + \delta\boldsymbol{\eta}_{\mathrm{Ti}}(t)\cdot\nabla_{\boldsymbol{\eta}_{\mathrm{Ti}}}\mathcal{J} + \delta\boldsymbol{\eta}_{\mathrm{Er}}(t)\cdot\nabla_{\boldsymbol{\eta}_{\mathrm{Er}}}\mathcal{J}. \quad (14)$$

In Eq. (14), the first term describes a piezoelectric modulation of the Er-Ti bond, whereas the second terms describe direct RF-induced changes of the local orbital configurations which are determined by the coupling between the microwave and the atomic orbitals[11,12]. The piezoelectric contribution is in general a weak effect[3,11], and therefore we neglect this term. In addition, within a minimal description, the direct orbital-deformation terms mainly modulate the diagonal values of $\mathcal{J}$ ($\mathcal{J}_{xx}$, $\mathcal{J}_{yy}$ and $\mathcal{J}_{zz}$), and therefore they do not mix spin indexes.

To investigate the driving term involving the spin-index-preserving terms: i.e. $\boldsymbol{S}_{\mathrm{Ti}}^{x}\delta\mathcal{J}_{xx}\boldsymbol{S}_{\mathrm{Er}}^{x}$, $\boldsymbol{S}_{\mathrm{Ti}}^{y}\delta\mathcal{J}_{yy}\boldsymbol{S}_{\mathrm{Er}}^{y}$ and $\boldsymbol{S}_{\mathrm{Ti}}^{z}\delta\mathcal{J}_{zz}\boldsymbol{S}_{\mathrm{Er}}^{z}$, we calculate the ESR spectrum within linear response theory by treating the RF excitation as a weak time-dependent perturbation: $\mathcal{H}_{\mathrm{drive}} = \boldsymbol{S}_{\mathrm{Ti}}^{x}\delta\mathcal{J}_{xx}\cos(\omega_{\mathrm{RF}}t)\boldsymbol{S}_{\mathrm{Er}}^{x}$, $\mathcal{H}_{\mathrm{drive}} = \boldsymbol{S}_{\mathrm{Ti}}^{y}\delta\mathcal{J}_{yy}\cos(\omega_{\mathrm{RF}}t)\boldsymbol{S}_{\mathrm{Er}}^{y}$ and $\mathcal{H}_{\mathrm{drive}} = \boldsymbol{S}_{\mathrm{Ti}}^{z}\delta\mathcal{J}_{zz}\cos(\omega_{\mathrm{RF}}t)\boldsymbol{S}_{\mathrm{Er}}^{z}$ added to the static spin Hamiltonian $\mathcal{H}$. After diagonalizing $\mathcal{H}$, the absorption intensity at frequency ω_{RF} is obtained by summing over all allowed transitions between eigenstates $|n\rangle$ and $|m\rangle$,

$$I(\omega) \propto \sum_{n,m}(p_n - p_m)\left|\langle m|\,\mathcal{H}_{\mathrm{drive}}\,|n\rangle\right|^2 L\left[\omega - \frac{E_m - E_n}{\hbar}\right], \quad (15)$$

where $p_n \propto \exp(-E_n/k_{\mathrm{B}}T)$ is the Boltzmann population and $L(\omega)$ is a Lorentzian lineshape accounting for the finite linewidth, which we set to be 10 MHz. This approach directly connects the calculated ESR peak positions to the eigenenergy differences of $\mathcal{H}$, while the

peak intensities are determined by the transition matrix elements of the RF driving operator and the population difference between two levels. Here we neglect the tip polarization for the readout process, which does not qualitatively change the results. To compare with the experimental ESR map and Rabi frequencies as a function of polar angle θ (with ϕ fixed at 52°, Fig. S9**a**), we simulate ESR map and normalized Rabi frequencies (normalized by f_3 at $\theta = 90°$) by modulating the $\boldsymbol{S}^x_{\mathrm{Ti}}\delta\mathcal{J}_{xx}\boldsymbol{S}^x_{\mathrm{Er}}$, $\boldsymbol{S}^y_{\mathrm{Ti}}\delta\mathcal{J}_{yy}\boldsymbol{S}^y_{\mathrm{Er}}$ and $\boldsymbol{S}^z_{\mathrm{Ti}}\delta\mathcal{J}_{zz}\boldsymbol{S}^z_{\mathrm{Er}}$ terms. The ESR map and the normalized Rabi frequencies are presented in Figs. S9**b-c**, S10**a-b** and S11**a-b**. The simulation clearly fails to reproduce the key experimental observations:

- For the case of modulating $\boldsymbol{S}^x_{\mathrm{Ti}}\delta\mathcal{J}_{xx}\boldsymbol{S}^x_{\mathrm{Er}}$ (as in Fig. S9), the ESR intensity as well as the normalized Rabi frequencies are too strong compared with experimental results. In addition, the ESR intensity of f_3 shows almost no change when θ approaches 90°, while the experimental results show a clear decrease of ESR intensity when the field is aligned in the in-plane direction.

- For the case of modulating $\boldsymbol{S}^y_{\mathrm{Ti}}\delta\mathcal{J}_{yy}\boldsymbol{S}^y_{\mathrm{Er}}$ (as in Fig. S10), the ESR intensity of f_4 decreases when field goes in-plane, and the f_3 ESR peak shows no clear decrease when field goes in plane. More importantly, the normalized Rabi frequencies for DQT are twice as strong as in the experimental results.

- For the case of modulating $\boldsymbol{S}^z_{\mathrm{Ti}}\delta\mathcal{J}_{zz}\boldsymbol{S}^z_{\mathrm{Er}}$ (as in Fig. S11), the ESR peak intensities of f_1 to f_5 show all distinctly different trends compared with experimental results in Fig. S9**a** and the normalized Rabi frequencies cannot capture the experimental results.

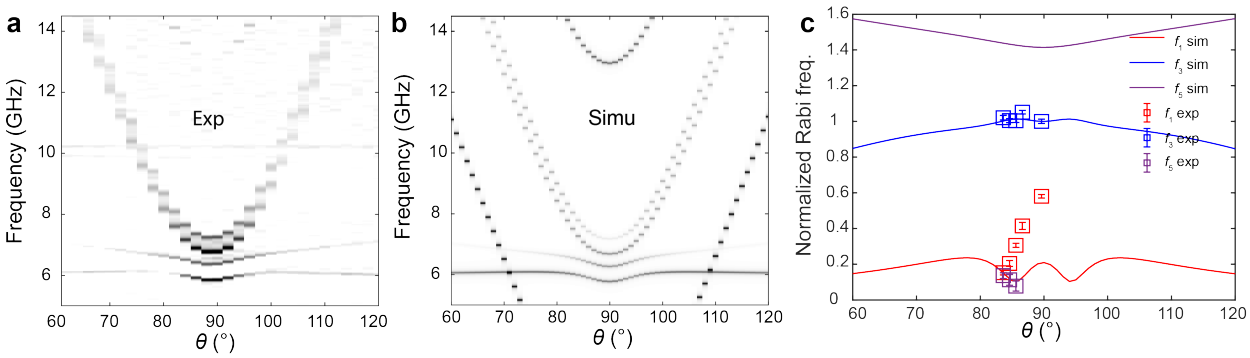

FIG. S9. **Modulation of the $S^x_{\mathrm{Ti}}\delta\mathcal{J}_{xx}S^x_{\mathrm{Er}}$ term in the (3,0) pair. a,** Experimental ESR map as a function of the polar angle θ ($\phi = 52°$, $V_{\mathrm{DC}} = 100$ mV, $I_{\mathrm{DC}} = 20$ pA, $V_{\mathrm{RF}} = 20$ mV). **b,** Simulated ESR map as a function of the polar angle θ ($\phi = 52°$). **c,** The normalized Rabi frequencies as a function of polar angle (normalized by the Rabi frequencies of f_3 at $\phi = 52°$ and $\theta = 90°$). The solid lines are simulations while the colored squares are the experimental results. All experimental data in (**c**) were acquired with $V_{\mathrm{DC}} = 100$ mV, $I_{\mathrm{DC}} = 20$ pA, $V_{\mathrm{RF}} = 100$ mV, $\boldsymbol{B}_{\mathrm{ext}} = 0.25$ T and $\phi = 52°$.

B. Modulating the off-diagonal term through rotational modulation

Since all the terms in Eq. (14) fail to account for the experimental observation, we therefore focus on the second part of Eq. (13), namely the spin-index rotation of the anisotropic exchange tensor: $\mathcal{H}_{\mathrm{rot}} = A^{\mathsf{T}}_{\mathrm{Ti}}(t)\mathcal{J} + \mathcal{J}A_{\mathrm{Er}}(t)$, which describes the local basis change when traveling along the trajectory and creates off-diagonal components in $\mathcal{J}(\boldsymbol{q}(t))$. Note that for a pure translational trajectory in the space of $\boldsymbol{q}$, $\mathcal{H}_{\mathrm{rot}}$ is zero, since it does not change the local spin basis of Er and Ti. We therefore consider the rotational trajectory. For a finite rotation, this tensorial part of the Lie derivative can be represented as

$$\mathcal{J} \to \mathcal{J}_{\mathrm{rot}}(t) = R^{\mathsf{T}}_{\mathrm{Ti}}(t)\mathcal{J}R_{\mathrm{Er}}(t), \tag{16}$$

where $R_{\mathrm{Ti}}(t)$ and $R_{\mathrm{Er}}(t)$ are $SO(3)$ rotation matrices acting on the Ti and Er spin indices. The corresponding RF-induced modulation of the exchange tensor is therefore

$$\delta\mathcal{J}_{\mathrm{rot}}(t) = R^{\mathsf{T}}_{\mathrm{Ti}}(t)\mathcal{J}R_{\mathrm{Er}}(t) - \mathcal{J}. \tag{17}$$

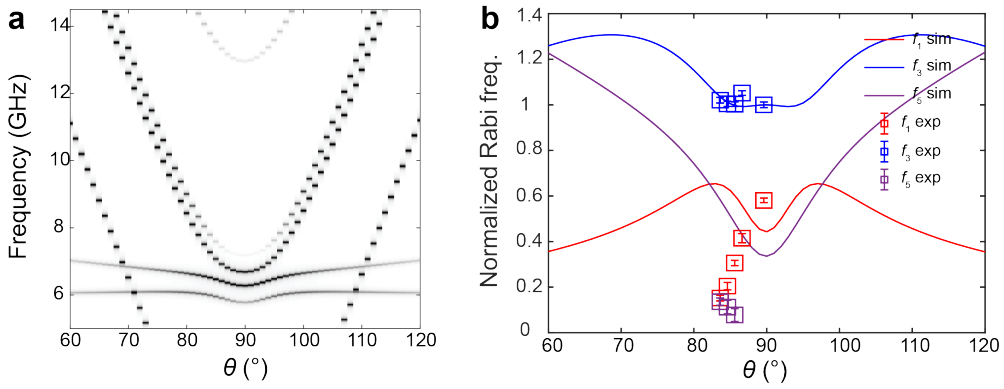

FIG. S10. **Modulation of the $S^y_{\mathrm{Ti}}\delta\mathcal{J}_{yy}S^y_{\mathrm{Er}}$ term in the (3,0) pair. a,** Simulated ESR map as a function of the polar angle θ ($\phi = 52°$). **b,** The normalized Rabi frequencies as a function of polar angle (normalized by the Rabi frequencies of f_3 at $\phi = 52°$ and $\theta = 90°$). The solid lines are simulation while the colored squares are the experimental results. All experimental data were acquired with $V_{\mathrm{DC}} = 100$ mV, $I_{\mathrm{DC}} = 20$ pA, $V_{\mathrm{RF}} = 100$ mV, $\boldsymbol{B}_{\mathrm{ext}} = 0.25$ T and $\phi = 52°$.

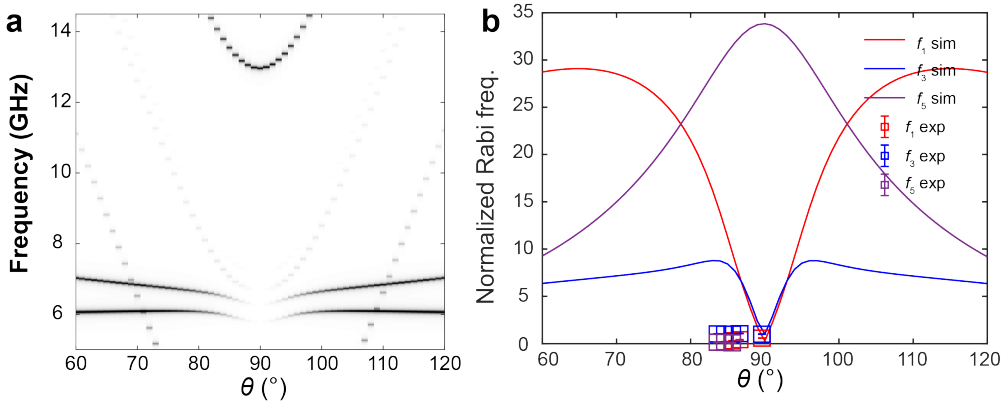

FIG. S11. **Modulation of the $S^z_{\mathrm{Ti}}\delta\mathcal{J}_{zz}S^z_{\mathrm{Er}}$ term in the (3,0) pair. a,** Simulated ESR map as a function of the polar angle θ ($\phi = 52°$). **b,** The normalized Rabi frequencies as a function of polar angle (normalized by the Rabi frequencies of f_3 at $\phi = 52°$ and $\theta = 90°$). The solid lines are simulation while the colored squares are the experimental results. All experimental data were acquired with $V_{\mathrm{DC}} = 100$ mV, $I_{\mathrm{DC}} = 20$ pA, $V_{\mathrm{RF}} = 100$ mV, $\boldsymbol{B}_{\mathrm{ext}} = 0.25$ T and $\phi = 52°$.

The associated driving Hamiltonian is based on the rotational modulation of $\mathcal{J}$:

$$\mathcal{H}_{\mathrm{rot}}(t) = \boldsymbol{S}_{\mathrm{Ti}}\delta\mathcal{J}_{\mathrm{rot}}(t)\boldsymbol{S}_{\mathrm{Er}}. \tag{18}$$

To minimize the energetic cost of the RF excitation, we consider the rotational mode of the local anisotropy frame that leaves the dominant Zeeman energy unchanged. Physically,

the RF electric field modulates the orbital structure that defines the principal axes of the $\mathfrak{g}$-tensor and the exchange tensor $\mathcal{J}^{\mathrm{exc}}$. Through spin-orbit coupling, this modulation is equivalently described as an apparent wobbling of the magnetic moments around the external field $\boldsymbol{B}_{\mathrm{ext}}$ (Fig. S12). Since this wobbling changes only the azimuthal direction of $\boldsymbol{\mu}_i$ while preserving its projection onto $\boldsymbol{B}_{\mathrm{ext}}$, the Zeeman energy is unchanged to leading order. For this energetically favorable mode, we first write Eq (18) in the form of magnetic moment ($\boldsymbol{\mu}_{\mathrm{Er(Ti)}} = \mu_{\mathrm{B}}\mathfrak{g}_{\mathrm{Er(Ti)}} \cdot \boldsymbol{S}$):

$$\mathcal{H}_{\mathrm{rot}} = \boldsymbol{\mu}_{\mathrm{Ti}}\mathcal{J}^{\mathrm{M}}\boldsymbol{\mu}_{\mathrm{Er}} \tag{19}$$

with $\mathcal{J}^{\mathrm{M}} = \mathfrak{g}_{\mathrm{Ti}}^{-1}\mathcal{J}\mathfrak{g}_{\mathrm{Er}}^{-1}/\mu_{\mathrm{B}}^2$. In this framework, we write:

$$R_{\mathrm{Ti}}(t) = R_{\mathrm{Er}}(t) = R_B[\delta\alpha(t)]\,, \tag{20}$$

where R_B is a rotation around $\boldsymbol{B}_{\mathrm{ext}}$, and

$$\delta\alpha(t) = \delta\alpha_0 \cos(\omega_{\mathrm{RF}} t) \tag{21}$$

is the RF-induced rotational modulation. Equation (17) then becomes

$$\delta\mathcal{J}^{\mathrm{M}}_{\mathrm{rot}}(t) = R_B^{\mathsf{T}}[\delta\alpha(t)]\,\mathcal{J}^{\mathrm{M}} R_B[\delta\alpha(t)] - \mathcal{J}^{\mathrm{M}}. \tag{22}$$

For small $\delta\alpha$, the rotation matrix can be expanded as

$$R_B[\delta\alpha(t)] = I + \delta\alpha(t) G_B + \mathcal{O}\big[\delta\alpha(t)^2\big]\,, \tag{23}$$

where G_B is the generator of rotations around $\hat{\boldsymbol{n}}_B$. Since G_B is antisymmetric,

$$G_B^{\mathsf{T}} = -G_B. \tag{24}$$

Substituting Eq. (23) into Eq. (22), we obtain

$$\begin{aligned}\delta\mathcal{J}^{\mathrm{M}}_{\mathrm{rot}}(t) &= [I - \delta\alpha(t)G_B]\,\mathcal{J}^{\mathrm{M}}\,[I + \delta\alpha(t)G_B] - \mathcal{J}^{\mathrm{M}} + \mathcal{O}\big[\delta\alpha(t)^2\big] \\ &= \delta\alpha(t)\left(\mathcal{J}^{\mathrm{M}}G_B - G_B\mathcal{J}^{\mathrm{M}}\right) + \mathcal{O}\big[\delta\alpha(t)^2\big]\,.\end{aligned} \tag{25}$$

Thus, to leading order,

$$\delta\mathcal{J}^{\mathrm{M}}_{\mathrm{rot}}(t) = \delta\alpha(t)\left[\mathcal{J}^{\mathrm{M}}, G_B\right], \tag{26}$$

The rotational driving Hamiltonian is therefore:

$$\mathcal{H}_{\mathrm{rot}}(t) = \mathcal{H}_1(t) = \delta\alpha(t)\boldsymbol{\mu}_{\mathrm{Ti}}\left[\mathcal{J}^{\mathrm{M}}, G_B\right]\boldsymbol{\mu}_{\mathrm{Er}}. \tag{27}$$

Equation (27) shows that the RF drive is controlled by the commutator between the anisotropic exchange tensor and the generator of rotations around the external magnetic field. Note Equation (27) is a generalized form of Eq. 2 in the main text that accounts for the $\mathfrak{g}$-tensor anisotropy of both spins. This term vanishes for an isotropic exchange interaction, $\mathcal{J}^{\mathrm{M}} = JI$, because in that case

$$\left[\mathcal{J}^{\mathrm{M}}, G_B\right] = 0. \tag{28}$$

Therefore, the anisotropy of $\mathcal{J}$ is essential for this driving mechanism.

The same result can be understood in the co-moving anisotropy frame. In this frame, the orbital landscape is static, while the magnetic moments appear to counter-wobble around $\boldsymbol{B}_{\mathrm{ext}}$ (as shown in Fig. S12):

$$\mathcal{H}_J(t) = \left[R_B(\delta\alpha(t))\,\boldsymbol{\mu}_{\mathrm{Ti}}\right]^{\mathsf{T}} \mathcal{J}^{\mathrm{M}} \left[R_B(\delta\alpha(t))\,\boldsymbol{\mu}_{\mathrm{Er}}\right]. \tag{29}$$

Equivalently, in spin-coordinate space this corresponds to the $\mathfrak{g}$-stretched rotations $W_i(t) = \mathfrak{g}_i^{-1} R_B(t) \mathfrak{g}_i$. Thus the "spin wobbling" picture is not a literal direct rotation of the spin by the microwave field, but an equivalent description of the RF-induced modulation of the orbital anisotropy frame.

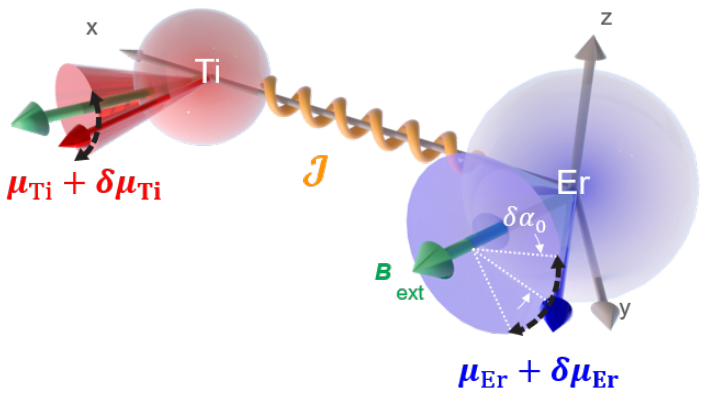

FIG. S12. **Wobbling the magnetic moment around the external magnetic field.** The rotational modulation of $\mathcal{J}$ can be viewed in the rotating frame as the wobbling of magnetic moment around the magnetic field $\boldsymbol{B}_{\mathrm{ext}}$. The change of Ti magnetic moment $\delta\boldsymbol{\mu}_{\mathrm{Ti}}$ will exert an oscillating field on the Er spin which drives the Er spin transitions. And similarly, the wobbling of the Er spin exerts an oscillating field on the Ti spin.

We simulate the ESR map using Eq. (27) and compare it with experimental results. In Figs. S13 and S14, we present the experimental and simulated ESR maps as a function of the polar angle θ, with ϕ fixed at 52°, for the (3,0) and (2.5, −0.5) Er-Ti spin pairs. In both cases, the experimental ESR maps exhibit clear and systematic trends as the polar angle is varied:

- For both the (3,0) and (2.5, −0.5) pairs, the DQT intensity diminishes as the polar angle approaches the in-plane direction (90°).
- For the (3,0) pair, the ESR transition intensities from f_1 to f_4 increase as the magnetic field approaches the in-plane orientation.

The simulated ESR maps based on our model of rotational modulation of the spin-spin coupling tensor reproduce these trends well, as shown in Fig. S13**b** and Fig. S14**c**. Furthermore, for the (3,0) pair, the model also captures the angular dependence of the Rabi frequencies, as presented in Fig. S13**c** where we show the Rabi frequencies, normalized to the f_3 Rabi frequency at $\theta = 90°$, as a function of the polar angle θ with ϕ fixed at 52°.

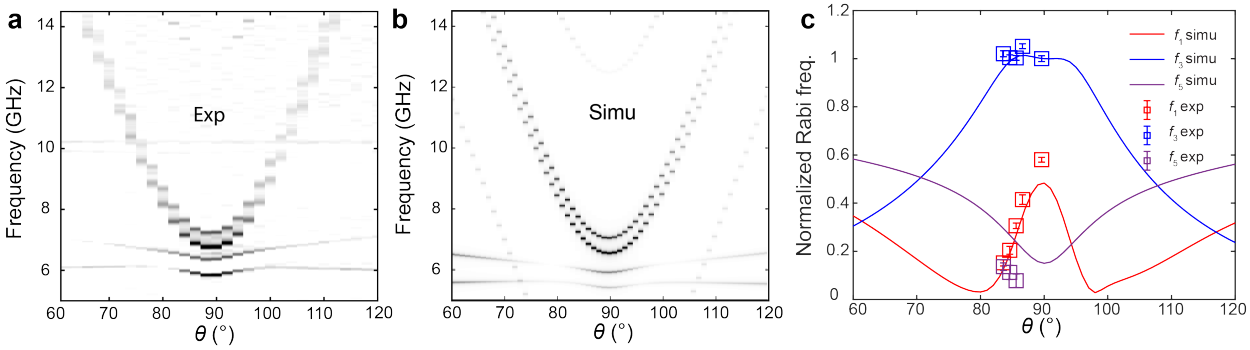

FIG. S13. **Simulation based on rotational modulation for the (3, 0) pair. a,** Experimental ESR map as a function of the polar angle θ ($\boldsymbol{B}_{\rm ext} = 0.25$ T, $\phi = 52°$, $V_{\rm DC} = 100$ mV, $I_{\rm DC} = 20$ pA, $V_{\rm RF} = 20$ mV). **b,** Simulated ESR map as a function of the polar angle θ ($\phi = 52°$) assuming a wobbling angle of $\delta\alpha_0 = 0.1\pi$. **c,** The normalized Rabi frequencies as a function of the polar angle (normalized by the Rabi frequencies of f_3 at $\phi = 52°$ and $\theta = 90°$). The solid lines are simulations while the colored squares are the experimental results. All experimental data in (**c**) were acquired with $V_{\rm DC} = 100$ mV, $I_{\rm DC} = 20$ pA, $V_{\rm RF} = 100$ mV, $\boldsymbol{B}_{\rm ext} = 0.25$ T, $\phi = 52°$.

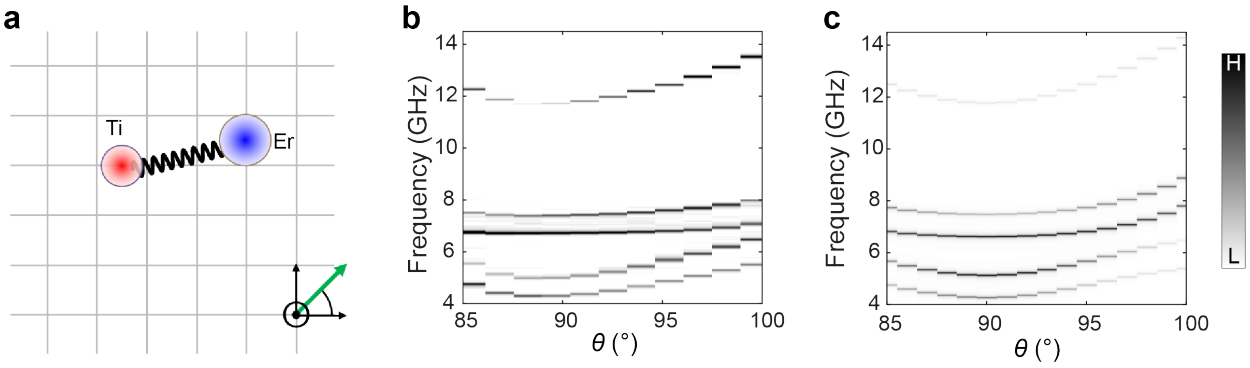

FIG. S14. **Simulation based on rotational modulation for the (2.5, −0.5) pair. a,** Schematic of the (2.5, −0.5) Er-Ti spin pair. **b,** Experimental ESR map as a function of the polar angle θ for the (2.5, −0.5) pair with ϕ fixed at 52° ($V_{\mathrm{DC}} = 100$ mV, $I_{\mathrm{DC}} = 20$ pA, $V_{\mathrm{RF}} = 20$ mV). **c,** Simulated ESR map as a function of the polar angle θ for the (2.5, −0.5) pair ($\phi = 52°$) assuming a wobbling angle of $\delta\alpha_0 = 0.1\pi$. All experimental data were acquired under the conditions of $\boldsymbol{B}_{\mathrm{ext}} = 0.25$ T, $\phi = 52°$.

C. Contribution of dipolar interaction

In this subsection, we evaluate the contribution of the dipolar interaction to the Rabi frequencies of f_1, f_3, and f_5 (normalized to the f_3 Rabi frequency at $\theta = 90°$, with ϕ fixed at 52°). As shown in Fig. S15, the exclusion of the dipolar interaction does not qualitatively modify the angular dependence of the Rabi frequencies as a function of the polar angle θ.

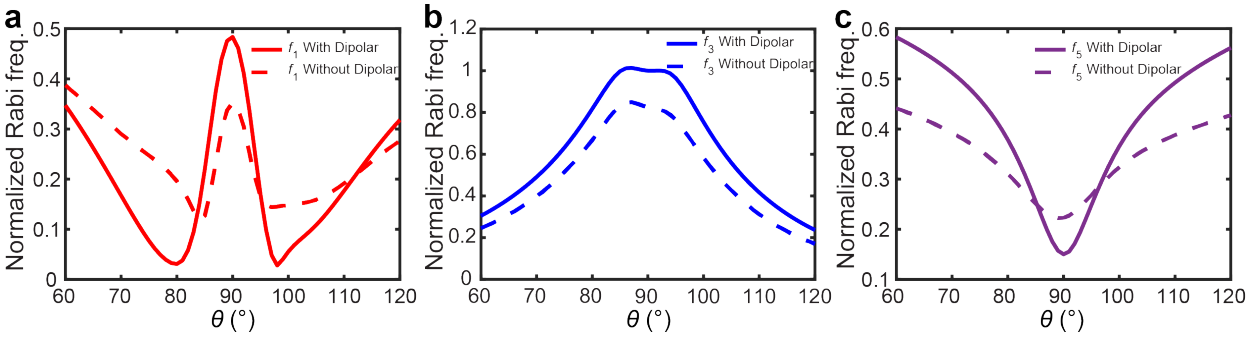

FIG. S15. **Contribution of the dipolar interaction to the Rabi frequency. a-c,** Normalized Rabi frequencies calculated with (solid lines) and without (dashed lines) the dipolar interaction as a function of the polar angle θ for f_1 (**a**), f_3 (**b**), and f_5 (**c**). All simulations were performed under an external magnetic field of $\boldsymbol{B}_{\text{ext}} = 0.25$ T with $\phi = 52°$ and a wobbling angle of $\delta\alpha_0 = 0.1\pi$.

D. Special cases of coherent control mechanism: $\theta = 90°$, $\phi = 0°$ or $\phi = 90°$

As shown in Fig. S16**a**, when the magnetic field is aligned along the x- or y-axis, both the Er and Ti spins are aligned with the field. In this configuration, rotational modulation around the magnetic-field direction does not modify the spin orientations and therefore does not produce any driving. Under these conditions, only the Ti transitions are detected as shown in Fig. S16**b**.

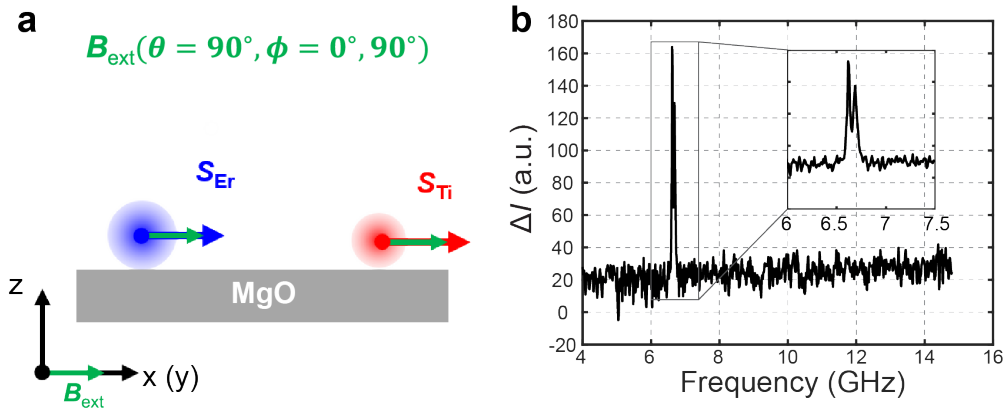

FIG. S16. **Special cases of the coherent control mechanism with $\boldsymbol{B}_{\text{ext}}$ aligned along the $\boldsymbol{x}$ or $\boldsymbol{y}$-axis. a,** Schematic illustration. When the magnetic field is aligned along an in-plane axis, both spins align with the field and therefore with each other. **b,** ESR spectrum measured at $\phi = 0°$ and $\theta = 90°$ ($\boldsymbol{B}_{\text{ext}} = 0.3$ T, $V_{\text{DC}} = 50$ mV, $I_{\text{DC}} = 20$ pA, $V_{\text{RF}} = 20$ mV). Only Ti transitions are observed.

E. Special cases of coherent control mechanism: $\theta = 90°$, $0° < \phi < 90°$

When the magnetic field is aligned in-plane ($\theta = 90°$) but with a finite azimuthal angle ϕ, the Er and Ti spins preferentially align closer to the y axis due to the in-plane $\mathfrak{g}$-tensor anisotropies. In this configuration, the wobbling of each magnetic moment around the magnetic-field direction induces a spin-vector variation with an out-of-plane component, as indicated by the yellow circle in Fig. S17. This generates an out-of-plane driving field $\boldsymbol{B}_1$.

The resulting $\boldsymbol{B}_1$ couples to the large out-of-plane $\mathfrak{g}$-tensor component $\mathfrak{g}_{zz}^{\mathrm{Er}}$ of the Er spin ($\mathfrak{g}_{zz}^{\mathrm{Er}} = 9.59$), which is substantially larger than the in-plane components. Consequently, this mechanism leads to the fast Rabi frequencies observed experimentally.

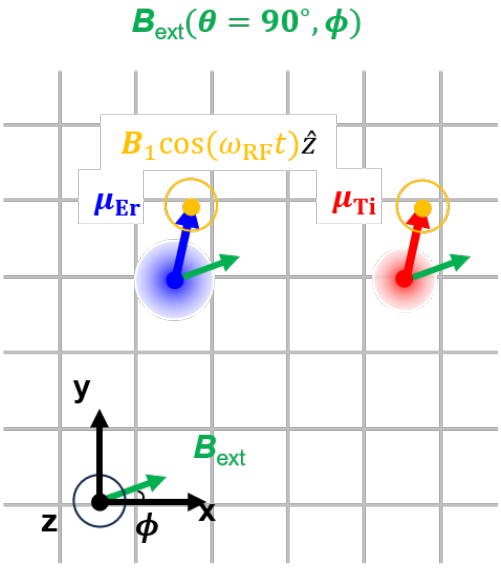

FIG. S17. **Special scenario of coherent control mechanism with $\boldsymbol{B}_{\mathrm{ext}}$ aligned in-plane $\theta = 90^{\circ}$ with $0^{\circ} < \phi < 90^{\circ}$.**

X. Readout process in Er-Ti pair

In this section, we discuss the readout process for the ESR measurement in Er(B)-Ti pair. In the case of Er(O)-Ti pair, where Ti and Er(O) spin have a lifetime imbalance[1] so that the spin pumping effect is taken into account for the read-out process. However, in the Er(B)-Ti pair, both spins have a comparable lifetime, on the order of 50 ns, yet one can still read out the Er spin states, even when Er and Ti have a substantial Zeeman energy difference (see Fig. 5 of the main text). Here we show that because of this rotational modulation of spin-spin interaction, even when two spins are in the Zeeman product state, one can still read out the Er-spin population change from Ti. This is because rotational modulation of spin interaction as shown by the driving Hamiltonian $\mathcal{H}_1$ (Eq. (27)) involves driving both spins simultaneously.

To simulate the ESR readout from the Ti spin in the coupled Er-Ti spin pair, we solve a Markovian master equation in Lindblad form for the driven open quantum system[13,14]. The static Hamiltonian includes the anisotropic Zeeman terms of the two spins in the external magnetic field together with their mutual interaction, using the Hamiltonian defined throughout this work (Eq. 1 of the main text). The numerical simulations are implemented using the Quantum Toolbox in Python (QuTiP)[15].

To incorporate relaxation and thermalization, we construct global thermal collapse operators using the strategy from previous studies on similar platforms[16,17] with the relaxation rates given by the T_1 of the Er and Ti spins measured from experiments (Section VII). In the absence of the RF drive, these dissipative terms relax the system toward the undriven thermal steady state at the chosen temperature $T = 1.0$ K. This undriven steady state is used as the initial density matrix for the continuous-wave ESR simulations. The driving Hamiltonian is given by Eq.(27). For each frequency f_{RF}, we solve the Lindblad equation in the time domain, discard the initial transient evolution, and then average the expectation value of the readout operator over the subsequent periodic steady-state regime. The readout operator is the tip polarization $\hat{\boldsymbol{P}}_{\mathrm{tip}}$, which is assumed to align with the magnetic field in accordance with the assumption that the tip field lies parallel or antiparallel to the external magnetic field. Repeating this procedure over the full frequency sweep yields the simulated ESR spectrum. To highlight the resonant contribution, we subtract an off-resonant back-

ground estimated from the spectral edges and normalize the resulting signal. The ESR peak positions therefore correspond to drive frequencies that resonantly enhance the change in the sensor readout, while the peak amplitudes reflect the strength of the driven response under the combined action of coherent driving and thermal dissipation.

In Fig. S18, we present the experimental and simulated ESR spectra using the model described above. The tip field is obtained from the fitting procedure described in Section III and the tip driving is modeled by $0.17\,\boldsymbol{S}_{\mathrm{Ti},x}$ to fit the experimental Ti transition peak heights (f_1 and f_2 in Fig. S18).

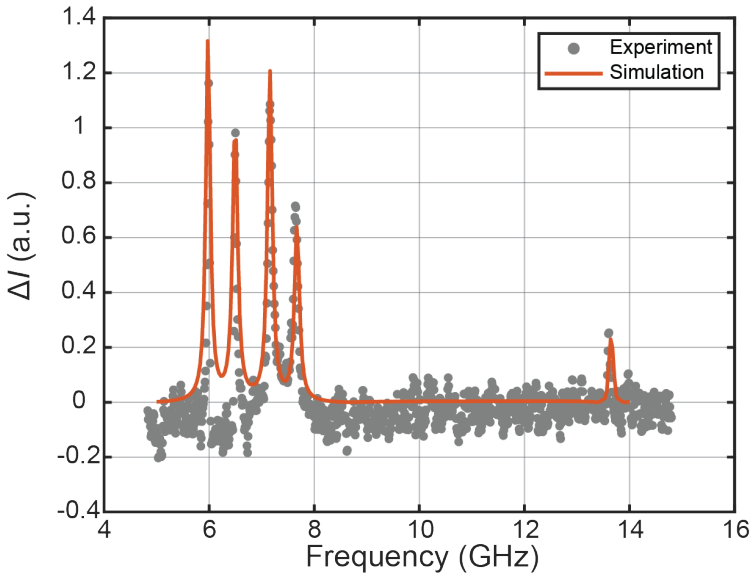

FIG. S18. **Simulated vs. experimental ESR spectra.** The gray circles represent the experimental data, while the red solid line represents the simulated ESR spectrum obtained using QuTiP. The readout operator is chosen as the tip polarization operator $\hat{\boldsymbol{P}}_{\mathrm{tip}}$, and the tip driving term is taken as $0.17\,\boldsymbol{S}_{\mathrm{Ti},x}$, which is chosen to reproduce the peak heights of the Ti transitions (f_1 and f_2). $\boldsymbol{B}_{\mathrm{ext}} = 0.25$ T, $\theta = 84.5°$, and $\phi = 52°$.

XI. Simulation of Er(O)-Ti pair

In this section, we apply our proposed mechanism to the Er(O)-Ti pair, where the Er atom is adsorbed on an oxygen binding site. As reported in previous work[1], the spin-spin interaction is $J_0 = 48$ MHz. In the effective spin-1/2 description obtained by projecting onto the ground-state doublet, the principal values of the $\mathfrak{g}$-tensor are $\mathfrak{g}_{xx}^{\mathrm{Er(O)}} = 9.6$, $\mathfrak{g}_{yy}^{\mathrm{Er(O)}} = 9.6$, and $\mathfrak{g}_{zz}^{\mathrm{Er(O)}} = 1.2$[1]. The simulated ESR transitions and Rabi frequencies as a function of the polar angle θ for different values of ϕ are presented in Fig. S19, assuming the same wobbling angle of $\delta\alpha_0 = 0.1\pi$. Comparing the Rabi frequencies of the Er transitions (f_3 and f_4 in Fig. S19) with those of the Ti transitions (f_1 and f_2 in Fig. S19), we observe that the Ti transitions exhibit higher Rabi frequencies.

Using the same rotational modulation model with the same wobbling angle $\delta\alpha_0 = 0.1\pi$, we compare the simulated Rabi frequencies between the Er(B)-Ti (3, 0) pair (Fig. S20) and the Er(O)-Ti pair (Fig. S19(**e**)) with the azimuthal angle $\phi = 45°$ and $\boldsymbol{B}_{\mathrm{ext}} = 0.32$ T. The Rabi frequencies for the Er(O)-Ti pair under the same condition are around 2 MHz as shown in Fig. S19(**e**), which are ∼30 times smaller than the case of the Er(B)-Ti (3, 0) under the same condition.

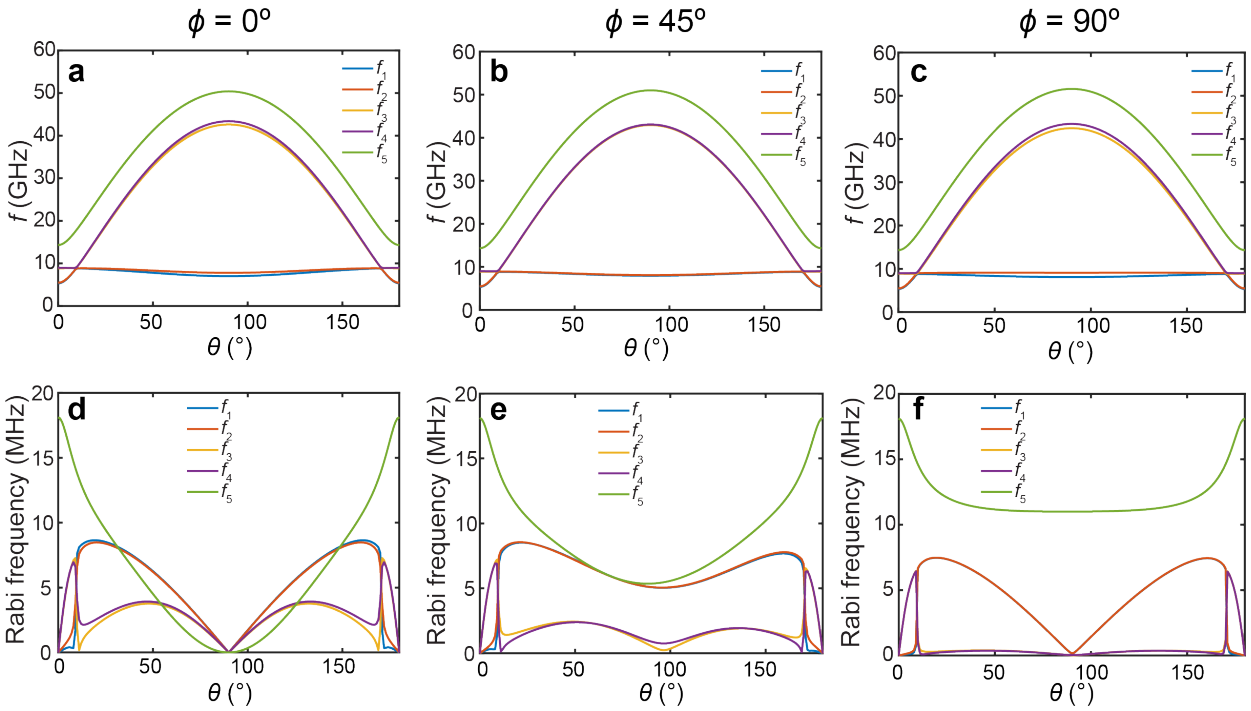

FIG. S19. **Simulation of Rabi frequencies and ESR transitions for the Er(O)-Ti pair in previous work[1]. a-c,** ESR transition for Er(O)-Ti pair as a function of polar angle θ for azimuthal angle of $\phi = 0°$ (**a**), 45° (**b**), 90° (**c**). **d-f,** Rabi frequency for Er(O)-Ti pair as a function of polar angle θ for azimuthal angle of $\phi = 0°$ (**d**), 45° (**e**), 90° (**f**). The simulation is done under the condition of $\boldsymbol{B}_{\text{ext}} = 0.32$ T as in the literature and we assume a wobbling angle of $\delta\alpha_0 = 0.1\pi$.

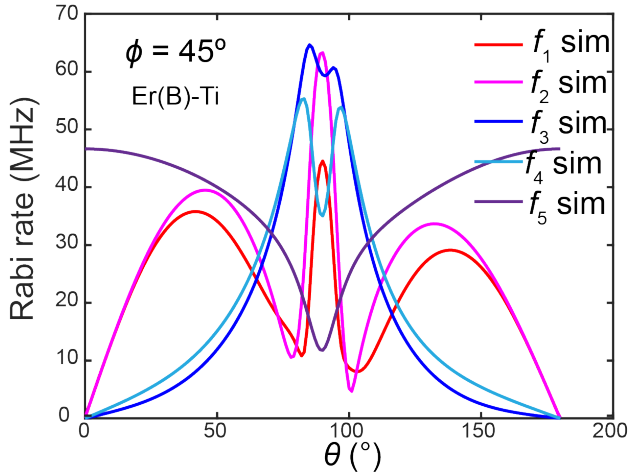

FIG. S20. **Simulation of Rabi frequencies for the (3, 0) Er(B)-Ti pair.** Rabi frequency for (3, 0) Er(B)-Ti pair as a function of polar angle θ. The simulation is done under the condition of $\boldsymbol{B}_{\text{ext}} = 0.32$ T and $\phi = 45°$ with $\delta\alpha_0 = 0.1\pi$.

* These authors contribute equally.

† liu.yaowu@qns.science

‡ phark@qns.science

§ donati.fabio@qns.science

[1] S. Reale, J. Hwang, J. Oh, H. Brune, A. J. Heinrich, F. Donati, and Y. Bae, Nature Communications **15**, 5289 (2024).

[2] K. Yang, Y. Bae, W. Paul, F. D. Natterer, P. Willke, J. L. Lado, A. Ferrón, T. Choi, J. Fernández-Rossier, A. J. Heinrich, *et al.*, Physical Review Letters **119**, 227206 (2017).

[3] S.-H. Phark, H. T. Bui, A. Ferrón, J. Fernández-Rossier, J. Reina-Gálvez, C. Wolf, Y. Wang, K. Yang, A. J. Heinrich, and C. P. Lutz, Advanced Science **10**, 2302033 (2023).

[4] M. W. Haverkort, in *Journal of Physics: Conference Series*, Vol. 712 (IOP Publishing, 2016) p. 012001.

[5] R. D. Cowan, *The Theory of Atomic Structure and Spectra*, Vol. 3 (University of California Press, 2023).

[6] S. Reale, A. Singha, S. Ahmed, D. Krylov, L. Colazzo, C. Wolf, C. Casari, A. Barla, E. Fernandes, F. Patthey, *et al.*, Physical Review B **107**, 045427 (2023).

[7] C. Görller-Walrand and K. Binnemans, Handbook on The Physics and Chemistry of Rare Earths **23**, 121 (1996).

[8] A. Uldry, F. Vernay, and B. Delley, Physical Review B—Condensed Matter and Materials Physics **85**, 125133 (2012).

[9] A. Singha, D. Sostina, C. Wolf, S. L. Ahmed, D. Krylov, L. Colazzo, P. Gargiani, S. Agrestini, W.-S. Noh, J.-H. Park, *et al.*, ACS Nano **15**, 16162 (2021).

[10] F. Donati, M. Pivetta, C. Wolf, A. Singha, C. Wackerlin, R. Baltic, E. Fernandes, J.-G. De Groot, S. L. Ahmed, L. Persichetti, *et al.*, Nano Letters **21**, 8266 (2021).

[11] J. Reina-Gálvez, H.-A. Le, H. T. Bui, S.-H. Phark, N. Lorente, and C. Wolf, Physical Review Research **7**, L042055 (2025).

[12] H. Maeda, D. Norum, and T. Gallagher, Science **307**, 1757 (2005).

[13] V. Gorini, A. Kossakowski, and E. C. G. Sudarshan, Journal of Mathematical Physics **17**, 821 (1976).

[14] G. Lindblad, Communications in mathematical physics **48**, 119 (1976).

[15] J. R. Johansson, P. D. Nation, and F. Nori, Computer Physics Communications **183**, 1760 (2012).

[16] H.-A. Le, S. Taherpour, D. Janković, and C. Wolf, npj Quantum Information (2026).

[17] R. Broekhoven, C. Lee, S.-h. Phark, S. Otte, and C. Wolf, npj Quantum Information **10**, 92 (2024).